UC San Diego
UC San Diego Previously Published Works

Title

Assimilating Global Wave Model Predictions and Deep-Water Wave Observations in Nearshore Swell Predictions

Permalink

Journal

ISSN

Authors

Crosby, Sean C
Cornuelle, Bruce D
O'Reilly, William C
et al.

Publication Date

DOI

Hurricane Imaging Radiometer (HIRAD) Wind Speed Retrievals and Validation Using Dropsondes

Daniel J. Cecil[1] and **Sayak K. Biswas**[2]

[1]NASA Marshall Space Flight Center, Huntsville, AL

[2]Universities Space Research Association, Huntsville, AL

Abstract

Surface wind speed retrievals have been generated and evaluated using Hurricane Imaging Radiometer (HIRAD) measurements from flights over Hurricane Joaquin, Hurricane Patricia, Hurricane Marty, and the remnants of Tropical Storm Erika, all in 2015. Procedures are described here for producing maps of brightness temperature, which are subsequently used for retrievals of surface wind speed and rain rate across a ~50 km wide swath for each flight leg. An iterative retrieval approach has been developed to take advantage of HIRAD's measurement characteristics. Validation of the wind speed retrievals has been conducted, using 636 dropsondes released from the same WB-57 high altitude aircraft carrying HIRAD during the Tropical Cyclone Intensity (TCI) experiment.

The HIRAD wind speed retrievals exhibit very small bias relative to the dropsondes, for winds tropical storm strength (17.5 m s^{-1}) or greater. HIRAD has reduced sensitivity to winds weaker than tropical storm strength, and a small positive bias (~2 m s^{-1}) there. Two flights with predominantly weak winds according to the dropsondes have abnormally large errors from HIRAD, and large positive biases. From the other flights, root mean square differences between HIRAD and the dropsonde winds are 4.1 m s^{-1} (33%) for winds below tropical storm strength, 5.6 m s^{-1} (25%) for tropical storm strength winds, and 6.3 m s^{-1} (16%) for hurricane strength winds. Mean absolute differences for those categories are 3.2 m s^{-1} (25%), 4.3 m s^{-1} (19%), and 4.8 m s^{-1} (12%), with bias near zero for tropical storm and hurricane strength winds.

1. Introduction

Mapping the surface wind speed in a hurricane is a great challenge that affects the ability to issue accurate forecasts and warnings for the maximum wind speed, wind field structure, and related impacts (Powell et al. 2009; Uhlhorn and Nolan 2012; Nolan et al. 2014). Buoys can provide useful measurements, but only for the precise parts of a hurricane that happen to track across the buoy. As with any surface stations, buoys are subject to failures in extreme conditions (i.e., the high winds and large waves of a hurricane). Satellite-based instruments typically are limited in heavy rain or very high wind speed conditions, or have coarse spatial resolution. Dropsondes from reconnaissance or research aircraft can provide detailed vertical profiles of the wind, but are necessarily limited in their coverage. The Stepped Frequency

Corresponding author: Daniel.J.Cecil@nasa.gov.

Microwave Radiometers (SFMR) on hurricane hunter aircraft are very good at estimating surface wind speed in hurricane conditions, but only along a nadir trace directly beneath the aircraft (Uhlhorn and Black 2003; Uhlhorn et al. 2007; Klotz and Uhlhorn 2014).

The Hurricane Imaging Radiometer (HIRAD) is an experimental four-channel, C-band, synthetic thinned array radiometer designed to *map* ocean surface wind speeds in hurricanes. Wind speed retrievals from HIRAD take advantage of the fact that the C-band emissivity of the ocean surface increases with increasing foam coverage, which results from wave breaking (Nordberg et al. 1971; Rosenkranz and Staelin 1972). Since the increase in foam is correlated with surface wind speed (Ross and Cardone 1974; Webster et al. 1976; Swift et al. 1984; Tanner et al. 1987), emissivity increases with surface wind speed. The sensitivity to wind speed is greatest at hurricane-force (> 33 m s^{-1}) and is therefore particularly useful for measuring the strongest winds. The four C-band channels also have varying sensitivity to rain, so rain rate and wind speed can be retrieved simultaneously. This concept is similar to that employed by the SFMR. Interferometric signal processing enables construction of a cross-track swath from HIRAD, such that the instrument functions as a pushbroom imager without mechanical scanning.

HIRAD has been flown on high-altitude aircraft (~20 km) in order to map ~50 km wide swaths from individual flight legs across hurricanes. In 2015, it overflew Atlantic Hurricane Joaquin, the remnants of Tropical Storm Erika, and Eastern North Pacific Hurricanes Patricia and Marty as part of the Office of Naval Research Tropical Cyclone Intensity (TCI) project (Doyle et al. 2017). Data processing methods and the production of wind speed retrievals from those flights are discussed in Sections 2 and 3. TCI also featured the High Definition Sounding System (HDSS) (Black et al. 2016), with dropsonde spacing sometimes less than 10 km. Quantitative comparison of HIRAD wind speed retrievals with near-surface wind speeds measured by dropsondes are discussed in Section 4.

2. HIRAD data processing and scene construction

a) Scene construction and calibration

In HIRAD there are ten antenna elements connected to ten dedicated receivers. Each of the antenna elements has a long, thin (fan beam) antenna pattern (Bailey et al. 2010) oriented in the cross-track direction relative to the heading of the platform. All ten fan beams overlap, defining a brightness temperature strip to be imaged. The pixels along the strip are resolved using synthetic antenna beams generated by interferometric techniques (Ruf et al. 1988). Forward motion of the platform creates a pushbroom imager, with a cross-track strip of data recorded approximately every second. This cross-track strip will be referred to as a scan, and the individual synthetic beam positions within the scan referred to as "scan positions". Nominal measurement characteristics are listed in Table 1.

The basic measurement of HIRAD is called a visibility vector, which consists of cross correlations (visibilities) of signals from all possible pairs of ten antenna elements. This includes the self-correlation, or zeroth visibility. The cross-track scene is reconstructed from those cross correlations. The zeroth visibility (or "Antenna Temperature" in traditional radiometry nomenclature) is a measurement of the average brightness temperature of the

cross-track scene weighted by the fan-beam antenna power pattern. The non-zero visibilities (cross-correlation between two *different* antenna elements) provide measurements of the perturbation of the scene about the mean (zeroth visibility). Depending on the spacing between pairs of correlating antenna elements, components of this perturbation with different spatial frequencies are sampled. The cross-track scene is reconstructed by combining the average value and the perturbations at 36 different spatial frequencies (similar to a Fourier reconstruction). The highest resolution possible for the image is determined by the highest spatial frequency sampled – which corresponds to the maximum possible distance between any two antenna elements in the HIRAD array.

Various types of error affect the image reconstruction procedure (Swift et al. 1991). The brightness temperature error for a given pixel in the cross-track scene can result from systematic offsets in the data and from random, zero-mean, measurement noise. The random component is a characteristic of the particular instrument design and is easily predicted. The systematic biases are harder to predict since they typically result from an incomplete or incorrect accounting of the sources of offset and gain corrections when calibrating the instrument. Temperature variations across the antenna are a major contributor to this. Although termed "systematic", they are not necessarily constant throughout a flight, or repeatable from one flight to the next. As the temperature variations evolve, so do these systematic errors.

For HIRAD, the systematic errors are much greater in magnitude than the random errors. Design considerations have been identified that could greatly reduce those errors in the future, but data from the current experimental version of the instrument require substantial postprocessing to reduce artifacts resulting from those errors.

The initial scene construction follows standard techniques for synthetic thinned array radiometers (Tanner and Swift 1993). The visibility vector is multiplied by the "Moore-Penrose pseudoinverse" (Penrose 1955) of the instrument's impulse response matrix (termed the "G matrix"). This G matrix was previously derived from measurements in an anechoic chamber and its pseudo inverse (Gp) was computed based on techniques discussed by Tanner and Swift (1993) and Goodberlet (2000). The cross track brightness temperature distribution obtained from the multiplication of Gp and V exhibits ripples as discussed by Ruf (1991). A combined effect of truncation of the lower visibility spectrum due to the antenna pattern envelope on the zeroth visibility interference pattern and inconsistencies between the different antenna element patterns produce these ripples. These ripples, along with the effect of synthetic antenna beam patterns, are compensated to produce a "true" brightness temperature image using a linear correction (antenna pattern correction) per pixel. The antenna pattern correction is derived from measurements of well-characterized hot and cold target scenes. A blackbody absorber during a pre-deployment calibration is used for the hot scene. For the cold target scenes, we use precipitation-free sections of flight legs over the ocean, selecting regions where winds are expected to be relatively weak and homogeneous. Multiple cold target scenes are selected for each flight, so the antenna pattern correction evolves during the flight to account for small calibration drifts. To characterize the cold target, a radiative transfer model is applied to an assumed surface state and atmospheric profile. The same radiative transfer model is used for the wind speed retrieval discussed in

section 3. The sea surface temperature is taken from the Multi-scale Ultra-high Resolution Sea Surface Temperature (https://mur.jpl.nasa.gov). Surface wind speeds for the cold calibration targets are taken from dropsondes, with wind speeds less than 7 m s^{-1}. A fixed atmospheric profile of temperature, water vapor, and cloud liquid water is taken from idealized numerical simulations of hurricanes described by Amarin et al. (2012). At HIRAD's C-band frequencies, sensitivity to realistic variations in these atmospheric profiles is small (Smith 1982; Tsang et al. 1977) compared to the instrument's measurement error. The scene construction and brightness temperature calibration is conducted separately for each of HIRAD's four frequencies.

HIRAD was built as a first prototype of an experimental instrument, to demonstrate the feasibility of a wide-swath, airborne, hurricane wind speed sensor. Non-ideal characteristics of its novel multi-frequency array antenna, a varying thermal environment during flight, and possibly an interaction with the aircraft radome combine to produce data with artificial along-track streaks where brightness temperatures are biased high or low. The magnitude of those streaks varies between channels, from flight to flight, and also within flight. This lack of consistency for the streaks makes them particularly difficult to objectively correct or remove. Some improvements in our initial scene construction procedure have made the streaks less prominent in the 2015 TCI HIRAD data than in data collected during previous field campaigns. The HIRAD measurement system includes some redundancies in zeroth and non-zero visibility measurements, and the radiometer passband for each frequency channel is divided into multiple subbands. Using optimal combinations of subbands and redundant visibilities does produce somewhat "cleaner" initial scenes. Of the ten HIRAD antenna elements, inconsistencies in the zeroth visibility time series were found associated with antenna 1, 6, 8, 9, and 10. Non-zero visibilities associated with those antennae are now preferentially rejected before image reconstruction, when redundant baselines involving other antennae are available. For each flight, subbands are now selected based on their consistency across all four frequencies. Earlier data from HIRAD's 4.0 GHz channel had been so dominated by streaks, that it previously appeared useless. With the improvements implemented for the 2015 TCI dataset, the 4.0 GHz channel is now incorporated in wind speed retrievals for the first time.

b) Smoothing and filtering

HIRAD was designed to sense only horizontally polarized (H-pol) emission from the target scene. Since the H-pol emissivity of the ocean surface decreases with increasing incidence angle, HIRAD's brightness temperature images are generally brightest near the nadir direction and the intensity decreases gradually away from nadir. This effect overwhelms the counter effect of a small increase due to longer atmospheric slant path for the pixels away from nadir. (The atmospheric contribution to measured brightness temperature is minimal at these C-band frequencies (Smith et al. 1982; Tsang et al. 1977).) The geophysical signature resulting from wind and rain gets modified by this systematic variation of cross track brightness temperature. As an attempt to compensate for this effect, an expected brightness temperature swath is computed using the radiative transfer model for a hypothetical clear, calm ocean scene with zero wind speed and no rain. This background scene is expected to have only the crosstrack variations that result from instrument viewing geometry for a

specular ocean surface. The background scene is subtracted from the measured scene to produce an array of "excess brightness temperatures" (Fig. 1), which *should* not have any systematic cross-track variability except that due to variability in the actual underlying scene. In the measured data, these excess brightness temperatures do exhibit cross-track variability due to the streaks mentioned in the previous subsection.

An ad hoc filtering was developed that treats each flight leg and each frequency separately. For each cross-track scan position (0 on the left, 320 on the right), the mean value of excess brightness temperature is computed for the entire flight leg. Then the fractional relative bias is computed for each scan position. This is the bias for a given scan position, divided by the mean excess brightness temperature of the other scan positions. Because HIRAD measurements carry the least uncertainty near the center of the swath, this bias is computed relative to the mean of the innermost 107 (out of 321 total) scan positions (that is, the innermost +/− 19°). Each scan position is then assigned a weight, inversely proportional to the absolute value of the fractional relative bias. Streaks (scan positions with systematically high or low biases) are thus given little weight in the subsequent smoothing. Scan positions with little bias would have weight approaching infinity, but for practical application the weight is limited to a value of 10 (Fig. 2a).

The weighting based on each scan position's relative bias is then combined with a Gaussian spatial smoothing using 41 pixels (+/− 20 left and right) in the cross-track direction (Fig. 2b). A stronger spatial smoothing is applied for the 4.0 and 5.0 GHz channels than for the 6.0 and 6.6 GHz channels, because the lower frequency channels tend to have a greater number of prominent streaks in the initial data, with smaller spacing between those streaks. The stronger smoothing essentially allows the filter to look further away from a given scan position to find relatively good (low biased, heavily weighted) data to include in the solution.

Consider scan position 130 in Fig. 2, which is 10.6° left (southwest) of the center of the flight track in Fig. 1. Here the value for the 4.0 GHz weighting function is 0.84 in Fig. 2a, one of the smallest values anywhere, because this scan position corresponds to a prominent streak in Fig. 1a. For scan position 130 in Fig. 2b (the top strip, for 4.0 GHz), neighboring pixels about 10–20 scan positions to the left and 10–20 scan positions to the right contribute more to the smoothed, filtered excess brightness temperature than scan positions very near 130 do. For scan position 195, on the other hand, the opposite is true. The weighting function in Fig. 2a maxes out at 10.0, so pixels very near scan position 195 contribute most to the smoothed, filtered solution there.

For the 6.6 GHz channel, the bias-related weighting function is near 10.0 (red line in Fig. 2a) for most of the swath, indicating that most of the streaks are low amplitude and do not need much correction. The spatial Gaussian filter then dominates the solution in the bottom strip of Fig. 2b. The main exception for 6.6 GHz is around scan position 37, viewing 49° left of the center of the flight track, where a prominent positive bias can be seen in Fig. 1d.

This smoothing is applied to instrument data that are strongly over-sampled relative to horizontal resolution (Table 1). The spacing between measurements is only a few hundred

meters, but the footprint size (i.e., the size of a synthetic antenna beam) for those measurements is a few km in each direction. Because the raw data are so strongly oversampled, the effective footprint size after smoothing is only slightly larger than before smoothing, except near the edges of the swath (Table 1 and Fig. 3).

The effect of the smoothing is demonstrated by comparing the initial excess brightness temperatures (Fig. 1) to the filtered, smoothed excess brightness temperatures (Fig. 4). The background brightness temperature that was originally subtracted is ultimately added back to the filtered, smoothed excess brightness temperatures. This yields the final quality controlled brightness temperatures that are used for wind speed and rain rate retrievals.

3. Retrieval approach

Our preferred retrieval approach is to construct simultaneous maximum likelihood estimates (MLE) of surface wind speed and column-averaged rain rate. This can be done by minimizing the difference between a vector of measured brightness temperatures at HIRAD's four frequencies, and a vector of modeled brightness temperatures from an ensemble of possible wind/rain combinations (Amarin et al. 2011). The treatment of surface emissivity as a function of wind speed follows the model of El-Nimri et al. (2010). The microwave absorption by rain follows Klotz and Uhlhorn (2014), using their Equation 12 and the revised coefficients listed in their Table 3. The surface emissivity and rain absorption models are consistent with the operational algorithm for the SFMR (Klotz and Uhlhorn 2014). The surface emissivity model also factors in incidence angle and polarization effects for HIRAD (El-Nimri et al. 2010). Since the surface emissivity models used for SFMR and HIRAD are based in part on estimates of 1-minute mean wind speed derived from dropsondes, the retrieved winds can be interpreted as 1-minute mean estimates. There is considerable uncertainty in what scales are truly being resolved by any of these radiometer or dropsonde measurements. Morris and Ruf (2015) additionally describe accounting for HIRAD's slant path view through an inhomogeneous rain field. The complication of *varying* rain along the slant path is not accounted for in the retrievals presented here, but it may be incorporated with future algorithm improvements. The length of the slant path through the rain layer is accounted for, after assuming that liquid rain extends 5 km in the vertical.

Ice particles are neglected in the radiative transfer model, as emission is negligible at these frequencies and scattering should be negligible in all but the rarest of cases. If ice scattering does occur, it would preferentially reduce brightness temperatures in the higher frequency channels, which would be misinterpreted as a reduction in rain rate. The best observational assessment we can make for potential ice scattering effects involves the Advanced Microwave Precipitation Radiometer (AMPR), which has flown on the NASA ER-2 with comparable altitudes and comparable spatial resolution as HIRAD on the WB-57. Cecil et al. (2010) mentioned that a slight scattering signature could even be seen in AMPR's lowest frequency (10.7 GHz) channel upon close inspection of data from Hurricane Emily (2005). Given that HIRAD's highest frequency channel has >60% longer wavelength (4.5 cm, versus 2.8 cm for AMPR's 10.7 GHz channel) we doubt that HIRAD would have been compromised by ice scattering. That Hurricane Emily case is thought to have the most intense convection of any hurricane case documented using high-altitude (~20 km) aircraft

(Cecil et al. 2010; Heymsfield et al. 2010). Leppert and Cecil (2015) did show 10.7 GHz ice scattering reducing the AMPR brightness temperatures up to about 40 K in Oklahoma severe thunderstorms. HIRAD's frequencies could conceivably be useful for identifying large hail in severe thunderstorms, but comparable conditions are exceedingly rare in hurricanes.

Conceptually, the retrieval should account for strong winds generating foam on the sea surface and raising the brightness temperatures in all C-band frequencies, and absorption/ emission by liquid rain drops preferentially raising the brightness temperatures in the higher frequency channels. Looking at the smoothed, filtered excess brightness temperatures in Fig. 4, one would expect most of the flight leg to have substantial surface wind, because brightness temperatures are elevated in all four channels. The quasi-circular eyewall near the southeast end of the leg likely has a combination of very strong wind and heavy rain, with elevated brightness temperatures in all channels and a greater enhancement in the highest frequencies. A more linear band (oriented from southwest to northeast) near the far southeast end of the flight leg is likely dominated by heavy rain, with its signal much stronger in the high frequency channels than the lower frequency channels.

Morris and Ruf (2015) showed rain rate retrievals from HIRAD, but noted that wind speed retrievals are more problematic because of sensitivity to the calibration. In our initial attempts to simultaneously retrieve wind speed and rain rate, the solutions are especially sensitive to relative calibration differences between the highest and lowest frequency channels used. If the 4.0 GHz channel is biased low relative to the 6.6 GHz channel, the retrieval will interpret this as a scene with mostly rain and little wind. The opposite is true if the 4.0 GHz channel is biased high, relative to the 6.6 GHz channel. The same pattern holds true if any combination of two, three, or four channels is used for the retrieval, with the solution being dominated by the relative differences between highest and lowest frequency channels.

The streaks discussed in Section 2, and imperfections in their removal, lead to patterns of relative calibration biases when comparing two or more channels. As such, the initial retrievals tend to alternate in unrealistic ways between interpreting a signal as being from very heavy rain with little wind, or very strong wind with no rain. The result can be a checkerboard pattern. A constrained MLE approach (Linwood Jones, personal communication, 2016) in which values for one scan are only allowed to change by some reasonable amount from the previous scan helps alleviate the problem of unrealistically alternating between light and strong wind.

Since more elegant retrieval approaches are not effective with the noisy measurements, we developed an iterative approach that combines simpler individual retrievals. Basically we conduct a sequence of single-channel retrievals, with the results from one retrieval constraining the possible solutions from the next retrieval.

- First, we run single-channel MLE retrievals for each channel, constraining the wind speed at a given scan position to change by no more than 1.5 m s^{-1} from one scan to the next. The 1.5 m s^{-1} value is somewhat arbitrary, but allows a realistic limit on the wind speed gradient (7.5 m s^{-1} km^{-1} in the along-track direction) in the initial retrievals. The resulting wind speeds subjectively look

credible (but probably biased a bit low) from the 4.0 GHz and 5.0 GHz retrievals. Wind speed retrievals from 6.0 GHz and 6.6 GHz subjectively look biased too low, with too much retrieved rain.

- Second, for each pixel we take the maximum value of the wind speed retrievals from 4.0 GHz and 5.0 GHz, calling this MaxWS45. We then re-run the single channel retrievals separately for 6.0 and 6.6 GHz, but constrain those retrievals to use MaxWS45 as the minimum possible wind speed solution for a given pixel. This allows the higher frequency channels to refine the wind speed estimate, and with their better effective spatial resolution they can refine the horizontal wind speed map.

- Third, for each pixel we take the mean of the 6.0 and 6.6 GHz wind speed retrievals, calling this MeanWS67.

- Fourth, the final wind speed product for each pixel (FinalWS) is computed as the mean of MaxWS45 and MeanWS67.

- Finally, we re-run a retrieval of rain rate only, providing that retrieval with FinalWS and the 6.6 GHz brightness temperature as inputs. This yields a rain rate pattern that takes advantage of the channel with the most responsiveness to rain, but is physically consistent with the wind speed that was derived from the previous steps.

This iterative approach is certainly not the most elegant, and we do not necessarily recommend using it for other instruments or for future data from HIRAD after improvements to the instrument hardware are made. It is a novel approach that provides useful maps of hurricane wind speed from the imperfect data that have already been collected.

4. Comparison with dropsondes

Retrieved HIRAD wind speeds (Cecil et al. 2016) were compared with near surface wind speed estimates from 636 HDSS dropsondes (Bell et al. 2016) in TCI flights over Hurricane Joaquin (2015), Hurricane Marty (2015), Hurricane Patricia (2015), and the remnants of Tropical Storm Erika (2015). Some of the flights over Marty and Patricia were at the tropical storm stage, with subsequent flights at hurricane stage. Doyle et al. (2017) summarize the TCI flights and datasets. From the quality controlled dropsonde wind profiles, a layer-average wind speed is computed over the lowest 150 m of the profile (WL150), or the lowest 500 m (MBL, for mean boundary layer) if low level data are unavailable (Franklin et al. 2003). This averaging removes some of the effect of gustiness in the dropsonde wind profile. Near surface wind speed is estimated from WL150 using the coefficients in Uhlhorn et al.'s (2007) Fig. 2. Otherwise it is estimated as 80% of the MBL value, following Franklin et al. (2003). Comparisons were made using any dropsonde that supported such a surface wind estimate, with its lowest reported location within the +/−60° swath from HIRAD.

For comparisons between HIRAD and dropsonde winds, the HIRAD wind speed retrievals are averaged over 500-m radius from the lowest reported location of the dropsonde. We have

not accounted for storm motion in these comparisons. The dropsonde takes about 10–15 minutes to reach the surface, after being released from nearly 20 km altitude. The tropical cyclone itself could translate several km during that time, with smaller scale features translating further if moving near the speed of local winds. Some of the largest differences between the HIRAD and dropsonde wind estimates appear to result from these storm motion effects, coupled with tight gradients of wind speed near the eyewall.

Scatterplots of HIRAD versus dropsonde wind speed estimates are stratified by flight (Fig. 5a) and incidence angle (Fig. 5b) in order to check for any obvious, consistent biases. HIRAD retrievals from the Hurricane Patricia 21 October flight do appear high biased, with several points having 25–45 m s^{-1} retrieved by HIRAD where the dropsondes indicate less than 20 m s^{-1} winds. The flight over the remnants of Tropical Storm Erika also had substantial high bias (the blue points toward the lower-left of Fig. 5a), which was expected because HIRAD has low sensitivity to weak wind speeds. Our retrievals artificially set a minimum wind speed at 10 m s^{-1}, because of this known low sensitivity to weak winds. Data from the other flights are generally scattered within 20% of the one-to-one line, other than outliers at low wind speeds (especially where dropsondes indicate < 20 m s^{-1} wind). Other than the Patricia 21 October flight, the largest differences are associated with drops in the eye of Hurricane Patricia on 23 October and Hurricane Joaquin on 4 October, with retrieved wind speeds around 40 m s^{-1} and dropsonde wind speeds < 20 m s^{-1}. These dropsondes splashed where HIRAD depicts a strong gradient between the eye and eyewall. Two of these are seen in the northern part of the eye/eyewall interface region in Fig. 6a. Based on 7 m s^{-1} storm motion from Hurricane Patricia's best track, the eye may have translated about 5 km further north-northeast while the sondes were falling. That would place these sondes (and similarly, the sonde from Hurricane Joaquin on 4 October) in the low-wind center mapped by HIRAD. The retrieved winds there are still too strong, likely because of the sea surface being roughened in this small eye itself, and because HIRAD has little sensitivity below about 15 m s^{-1}.

Although the purpose of this paper is to document the wind speed retrievals, the corresponding rain rate retrieval for the 23 October Hurricane Patricia flight is also mapped in Fig. 6c. For perspective, an 89-GHz satellite image is included in Fig. 6d. We suspect the rain retrievals are effective at distinguishing between moderate and heavier rain rates, but have not performed a quantitative evaluation. In this particular case, the retrieved rain rates have maxima in the northwest and southeast portions of the eyewall, immediately upwind and downwind of the retrieved wind speed maximum on the southwestern side. The retrieval could be assigning too much rain and not enough wind in the locations of the rain maxima, too much wind and not enough rain in the location of the wind maximum, or some combination of the two. The extreme wind speeds retrieved by HIRAD near 2100 UTC 23 October (76 m s^{-1}) are plausible, given best track estimates of 180 kt (93 m s^{-1}) at 1800 UTC and 130 kt (67 m s^{-1}) during landfall at 2300 UTC. The nadir-viewing SFMR on a NOAA P3 aircraft retrieved 67 m s^{-1} in the southeastern quadrant at 2033 UTC, with its flight track offset about 10 km from the portion of the swath with HIRAD's peak winds (Rogers et al. 2017).

Statistics from the HIRAD versus dropsonde comparisons are listed separately for each flight in Table 2. As described above, the flights over Tropical Storm Patricia on 21 October and the remnants of Tropical Storm Erika on 30 August have larger differences and much larger biases than the other flights. Most flights had small positive biases (less than 2 m s^{-1}), with root mean square differences around 6 m s^{-1} and mean absolute differences around 4 m s^{-1}. The biases are smallest over the range of tropical storm strength wind speeds (Table 3). The differences are largest in magnitude where HIRAD indicates hurricane strength winds, but the percentage difference is smallest for hurricane strength winds and largest for wind speeds weaker than tropical storm strength. Excluding the two problematic flights brings the bias below 2 m s^{-1} for all ranges of wind speed, and reduces the other error statistics noticeably. Further excluding the three eye dropsondes that were described above, where large differences are probably related to storm motion while the dropsondes fall, virtually eliminates the bias associated with hurricane strength wind speeds (Table 4). That also reduces the root mean square difference (mean absolute difference) for the remaining sample to 5.0 m s^{-1} (3.8 m s^{-1}), and for hurricane strength winds reduces those differences to 6.3 m s^{-1} (4.8 m s^{-1}).

No bias related to incidence angle is apparent in Fig. 5b. The high wind speeds in this comparison are mostly at high incidence angles, and low wind speeds at low incidence angles. But that is a result of high wind speeds carrying the dropsondes far to the side of the flight track, where HIRAD views with a high incidence angle. The few data points with a high wind speed retrieved at low incidence angle, or low wind speed at high incidence angle, do fall near the one-to-one line.

5. Summary, Discussion, and Future Directions

Data processing, smoothing/filtering, and surface wind speed retrieval techniques are described here for data collected by HIRAD in the 2015 TCI field experiment. Validation of the wind speed retrievals is presented using nearly coincident measurements from 636 dropsondes. HIRAD is an experimental instrument that maps scenes of C-band microwave brightness temperatures, with about 50 km swath width when flown around 20 km altitude. Surface wind speed is derived from those brightness temperatures, based on relationships between surface wind speed, resulting foam coverage on the ocean surface, and ocean surface microwave emissivity. HIRAD's four frequencies between 4.0 and 6.6 GHz are used to account for microwave emissions from liquid rain while retrieving surface wind speed.

Imperfections in the initial measurements must be accounted for in order to produce useful wind speed retrievals. Smoothing and filtering techniques described in Section 2b are designed to rely most on those parts of the measurements that exhibit the least noise for a given flight leg. An iterative wind speed retrieval technique described in Section 3 then uses the two lower frequency channels (4.0 and 5.0 GHz) to generate a first guess wind field. This constrains subsequent retrievals using the higher frequency (6.0 and 6.6 GHz) channels that provide more spatial detail. This approach is a compromise between more elegant approaches used with the operational, nadir-viewing SFMR (Klotz and Uhlhorn 2014), and practical considerations associated with experimental instrumentation.

The comparison between HIRAD- and dropsonde-derived surface wind speeds is quite encouraging. Flights over two of the weakest systems had abnormally large errors – the 30 August flight over the remnants of Tropical Storm Erika, and the 21 October flight over Tropical Storm Patricia. The current HIRAD antenna has low sensitivity to wind speeds below about 15 m s^{-1}, so confidence was low for those flights anyway. The HIRAD retrievals have a small positive bias (~2 m s^{-1}) at wind speeds less than tropical storm strength (17 m s^{-1}), in part because the retrieval artificially assumes at least 10 m s^{-1} wind everywhere.

Excluding the two aforementioned flights with abnormally large errors, and three dropsondes where the comparisons are especially compromised by storm motion during dropsonde descent, HIRAD's bias is near zero for tropical storm and hurricane strength winds. The root mean square difference between HIRAD- and dropsonde-estimated wind speed is around 5 m s^{-1}, and the mean absolute difference is around 4 m s^{-1}. Those values are higher in magnitude for hurricane strength winds (about 6 and 5 m s^{-1}, respectively), but in percentage terms the differences are lowest for hurricane strength winds (16% root mean square difference, 12 % mean absolute difference).

The validation of HIRAD wind speed retrievals has been presented here in terms of differences relative to dropsonde-based estimates, as distinct from being true error estimates. The root mean square difference in the HIRAD-versus-dropsonde comparisons results from HIRAD measurement and retrieval errors themselves, errors in the estimation of surface wind speed from the dropsondes, and the inherent variability of the true wind field. We consulted Nolan et al.'s (2013) Hurricane Nature Run and a simulation of a smaller, more intense storm provided by D. Nolan (Fig. 7) to estimate that spatiotemporal variability in the true wind field contributes ~2–3 m s^{-1} uncertainty to such comparisons. For uncertainty from the dropsonde-based surface wind speed estimates, we consider the 3.1 m s^{-1} root mean square difference reported in Fig. 3 of Uhlhorn et al. (2007). Using these values together with the 6.0 m s^{-1} root mean square difference in the HIRAD – dropsonde comparisons gives a rough estimate of root mean square error as $\mathrm{RMSE_{HIRAD}} = ((6.0 \text{ m s}^{-1})^2 - (3.1 \text{ m s}^{-1})^2 - (2 \text{ m s}^{-1})^2)^{0.5} = 4.7 \text{ m s}^{-1}$. Just as our HIRAD – dropsonde comparisons had differences exceeding 20 m s^{-1} in a few cases along the eyewall wind speed gradient, the simulation in Fig. 7d also has some differences exceeding +/–20 m s^{-1} in similar locations. While the largest differences relate to motion of the eye itself during the time it takes a dropsonde to descend, Fig. 7d also shows many locations where differences of a few m s^{-1} likely result from features rotating through the cyclonic flow. Merely removing a vortex-scale motion would not account for the cyclonic translation of smaller scale features. In practice, removing vortex-scale motion of a real hurricane is also difficult because short time scale "wobbles" of the eye are not captured by the best track.

The operational SFMR and its wind speed retrieval algorithm are considered the state of the art for this type of remote sensing, although the SFMR only measures a trace at nadir instead of mapping across a swath. The SFMR has been flown in hurricanes since 1980, with multiple generations of designs, hardware, and retrieval algorithms (Uhlhorn and Black 2003 and references therein; Uhlhorn et al. 2007; Klotz and Uhlhorn 2014). Klotz and Uhlhorn (2014) reported on the SFMR algorithm versions that were operational from 2006–2014

(termed "operational" in that paper), and the current version that became operational in 2015 (termed "revised" in that paper). The newer version reduced the SFMR bias for wind speeds below hurricane strength from 2–3 m s^{-1} to 0–1 m s^{-1}. Biases for hurricane strength winds were near zero for both versions. Root mean square difference versus dropsondes was reduced from 4.5 m s^{-1} (2006 version) to 3.9 m s^{-1} (2015 version), computed over the full range of wind speeds. Considering the SFMR's long history of frequent hurricane flights, HIRAD's relative youth (first flown in 2010, with flights over seven hurricanes through 2015), and the challenge of mapping a wide swath of winds, HIRAD's performance as documented here is promising.

Efforts are currently underway to improve HIRAD's measurement capabilities. A new antenna design has been tested, indicating that improved sensitivity to lower wind speeds can be achieved. Improvements to the integrated antenna – beamformer system, and to the thermal control, should reduce the raw measurement errors that currently necessitate a complicated retrieval approach. Even with the measurements that have already been collected, better retrievals might be achieved with certain modifications to our current approach. The spatial smoothing that is currently applied may be stronger than is necessary. Our MLE retrievals initially consider all possible combinations of wind speed and rain rate; historical SFMR retrievals or output from high resolution numerical models could be used to constrain which combinations of wind speed and rain rate are more likely to occur in nature.

Most of the interesting cases with data collected by HIRAD have been flown with the NASA WB-57 high altitude aircraft. Besides the flights used here from the 2015 TCI field experiment, there were three flights over Hurricane Gonzalo (2014) and one flight each over Hurricane Earl (2010) and Hurricane Karl (2010). The data processing and retrieval approaches described here could be applied to data from those flights, although there were no dropsonde-derived surface wind estimates for validation. In the future, flights on a high altitude, long endurance Global Hawk could conceivably provide wide swaths of wind speed (similar to those from WB-57) but with several repeated (or rotated) passes during a single mission. Alternatively, flights with HIRAD mounted on a lower altitude (~3 km) WP-3D aircraft would provide finer spatial resolution over a smaller swath width (~7 km). Instrumentation normally flown on the NOAA WP-3D during hurricanes would be suitable for addressing HIRAD's calibration and validation, improving the characterization of rain in the retrievals, and connecting the surface wind speed field with the wind field aloft as derived from Doppler radar.

Acknowledgments

References

Amarin RA, Jones WL, El-Nimri SF, Johnson JW, Ruf CS, Miller TL, Uhlhorn E. Hurricane wind speed measurements in rainy conditions using the airborne Hurricane Imaging Radiometer (HIRAD). IEEE Transactions on Geoscience and Remote Sensing. 2012; 50(1):180–192.

Bailey MC, Amarin R, Johnson J, Nelson P, James M, Sikmons D, Ruf C, Jones L, Gong X. Multi-Frequency Synthetic Thinned Array Antenna for the Hurricane Imaging Radiometer. IEEE Trans Ant & Prop. 2010; 58:2562–2570.

Bell, MM., Doyle, JD., Beaubien, M., Allen, T., Brown, BR., Dunion, J., Duran, P., Feldmeier, J., Harrison, LC., Hendricks, E., Jeffries, W., Komaromi, W., Martinez, J., Molinari, J., Moskaitis, J., Stern, DP., Vollaro, D. ONR Tropical Cyclone Intensity 2015 NASA WB-57 HDSS Dropsonde Data. Version 1.0. UCAR/NCAR - Earth Observing Laboratory; 2016. https://doi.org/10.5065/D6KW5D8M [Accessed 12 Apr 2016]

Black P, Harrison L, Beaubien M, Bluth R, Woods R, Penny A, Smith R, Doyle J. High Definition Sounding System (HDSS) for atmospheric profiling. J Atmos Oceanic Technol. 2016; in press. doi: 10.1175/JTECH-D-14-00210.1

Cecil DJ, Quinlan KR, Mach DM. Intense convection observed by NASA ER-2 in Hurricane Emily (2005). Mon Wea Rev. 2010; 138:765–780.

Cecil, DJ., Biswas, SK., Jones, WL., Alquaied, F. Hurricane Imaging Radiometer (HIRAD) Data. Version 2.1. UCAR/NCAR - Earth Observing Laboratory; 2016. https://doi.org/10.5065/D6CF9NGC [Accessed 4 Nov 2016]

Doyle, JD., et al. A View of Tropical Cyclones from Above: The Tropical Cyclone Intensity (TCI) Experiment. Bull Amer Meteor Soc, early online release. 2017. http://dx.doi.org/10.1175/BAMS-D-16-0055.1

El-Nimri SF, Jones WL, Uhlhorn E, Ruf C, Johnson J, Black P. An Improved C-Band Ocean Surface Emissivity Model at Hurricane-Force Wind Speeds Over a Wide Range of Earth Incidence Angles. IEEE Geosci Rem Sens Letters. 2010; 7:641–645.

Franklin JL, Black ML, Valde K. GPS dropwindsonde wind profiles in hurricanes and their operational implications. Wea Forecasting. 2003; 18:32–44.

Goodberlet MA. Improved image reconstruction techniques for synthetic aperture radiometers. IEEE Trans Geosci Rem Sens. 2000; 38:1362–1366.

Heymsfield GM, Tian L, Heymsfield AJ, Li L, Guimond S. Characteristics of deep tropical and subtropical convection from nadir-viewing high-altitude airborne Doppler radar. J Atmos Sci. 2010; 67:285–308.

Klotz BW, Uhlhorn EW. Improved stepped frequency radiometer tropical cyclone surface winds in heavy precipitation. J Atmos Oceanic Technol. 2014; 31:2392–2408.

Leppert KD II, Cecil DJ. Signatures of hydrometeor species from airborne passive microwave data for frequencies 10–183 GHz. J Appl Meteor Clim. 2015; 54:1313–1334.

Morris M, Ruf CS. A Coupled-Pixel Model (CPM) atmospheric retrieval algorithm for high-resolution imagers. J Atmos Oceanic Technol. 2015; 32:1866–1879.

Nolan DS, Atlas R, Bhatia KT, Bucci LR. Development and validation of a hurricane nature run using the joint OSSE nature run the WRF model. J Adv Model Earth Syst. 2013; 5:382–405. DOI: 10.1002/jame.20031

Nolan DS, Zhang JA, Uhlhorn EW. On the limits of estimating the maximum wind speeds in hurricanes. Mon Wea Rev. 2014; 142:2814–2837.

Nordberg WJ, Conaway J, Ross DB, Wilheit T. Measurements of microwave emission from a foam-covered, wind-driven sea. J Atmos Sci. 1971; 28:429–435.

Penrose R. A generalized inverse for matrices. Mathematical Proceedings of the Cambridge Philosophical Society. 1955; 51(3):406–413. DOI: 10.1017/S0305004100030401

Powell MD, Uhlhorn EW, Kepert JD. Estimating maximum surface winds from hurricane reconnaissance measurements. Wea Forecasting. 2009; 24:868–883.

Rogers, RF., Aberson, S., Bell, MM., Cecil, DJ., Doyle, JD., Morgerman, J., Shay, LK., Velden, C. Re-writing the tropical record books: The extraordinary intensification of Hurricane Patricia (2015).

Bull Amer Meteor Soc. 2017. early online release. DOI: http://dx.doi.org/10.1175/BAMS-D-16-0039.1

Rosenkranz PW, Staelin DH. Microwave emissivity of ocean foam and its effect on nadiral radiometric measurements. J Geophys Res. 1972; 77:6528–6538.

Ross DB, Cardone V. Observations of oceanic whitecaps and their relation to remote measurements of surface wind speed. J Geophys Res. 1974; 79:444–452.

Ruf CS. Error analysis of image reconstruction by a synthetic aperture interferometric radiometer. Radio Sci. 1991; 26:1419–1434.

Ruf CS, Swift CT, Tanner AB, Le Vine DM. Interferometric synthetic aperture microwave radiometry for the remote sensing of the earth. IEEE Trans Geosci Remote Sens. 1988; 26(5):597–611.

Smith EK. Centimeter and millimeter wave attenuation and brightness temperature due to atmospheric oxygen and water vapor. Radio Sci. 1982; 17:1455–1464.

Swift, CT., DeHority, DC., Black, PG., Chein, J-Z. Microwave remote sensing of ocean surface wind speed and rain rates over tropical storms. Frontiers of Remote Sensing of the Oceans and Troposphere from Air and Space Platforms: Proceedings of the URSI Commission F Symposium and Workshop, NASA Conference Publication; NASA; 1984. p. 281-286.

Swift CT, LeVine DM, Ruf CS. Aperture synthesis concepts in microwave remote sensing of the earth. IEEE Transactions on Microwave Theory and Techniques. 1991; 39(12):1931–1935.

Tanner, AC., Swift, CT., Black, PG. Operational airborne remote sensing of wind speeds in hurricanes. Preprints, 17th Conf. on Hurricanes and Tropical Meteorology; Miami, FL: Amer. Meteor. Soc; 1987. p. 385-387.

Tanner AB, Swift CT. Calibration of a synthetic aperture radiometer. IEEE Trans Geosci Rem Sens. 1993; 31:257–267.

Tsang L, Kong JA, Njoku E, Staelin DH, Waters JW. Theory for microwave thermal emission from a layer of cloud or rain. IEEE Trans Antennas Propag. 1977; 25:650–657.

Uhlhorn EW, Black PG. Verification of remotely sensed sea surface winds in hurricanes. J Atmos Oceanic Technol. 2003; 20:99–116. DOI: 10.1175/MWR-D-11-00073.1

Uhlhorn EW, Black PG, Franklin JL, Goodberlet M, Carswell J, Goldstein AS. Hurricane surface wind measurements from an operational Stepped Frequency Microwave Radiometer. Mon Wea Rev. 2007; 135:3070–3085. DOI: 10.1175/MWR3454.1

Uhlhorn EW, Nolan DS. Observational undersampling in tropical cyclones and implications for estimated intensity. Mon Wea Rev. 2012; 140:825–840. DOI: 10.1175/MWR-D-11-00073.1

Webster WJ Jr, Wilheit TT, Ross DB, Gloersen P. Spectral characteristics of the microwave emission from a wind-driven foam-covered sea. J Geophys Res. 1976; 81:3095–3099.
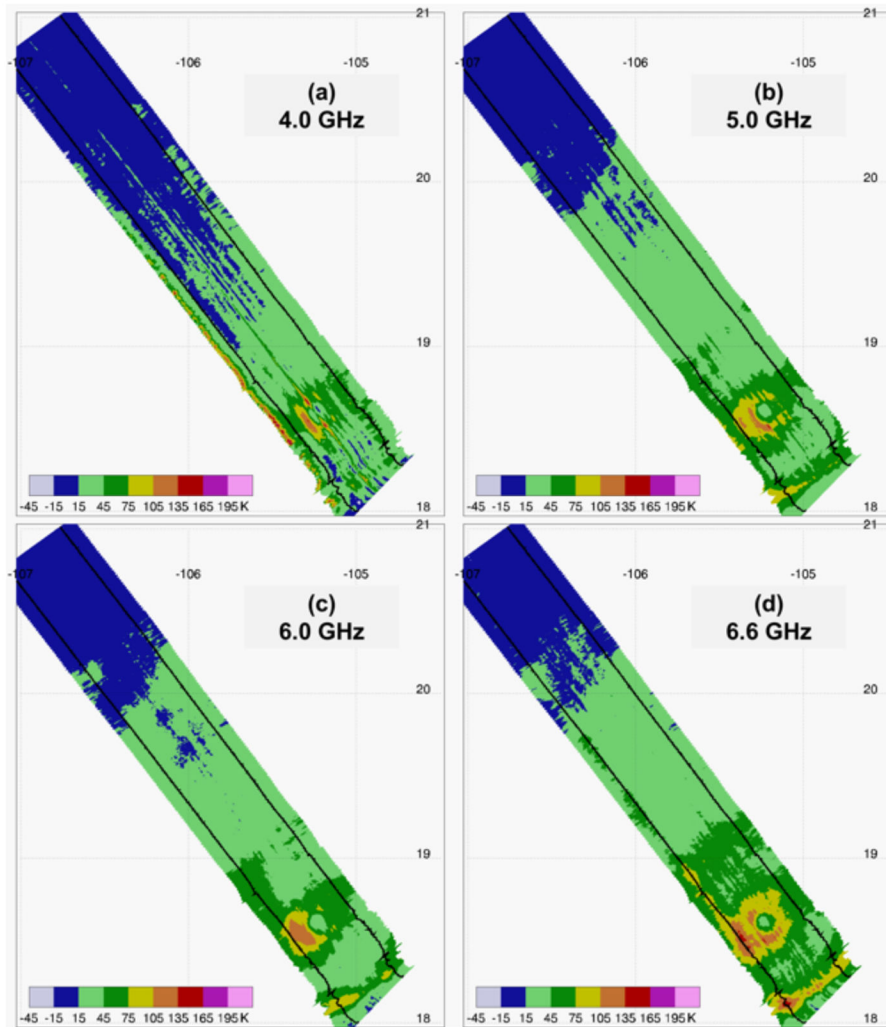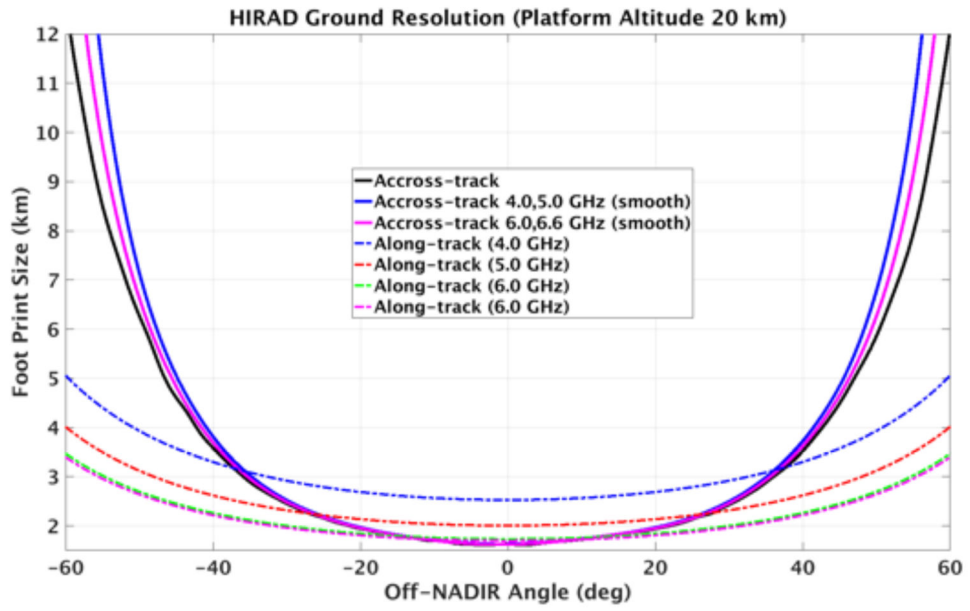
Figure 1.
Unfiltered, unsmoothed excess brightness temperatures at (a) 4.0, (b) 5.0, (c) 6.0, (d) 6.6 GHz for leg across Hurricane Patricia at 2001 UTC 23 Oct 2015. +/−60° swath is plotted. Solid black lines mark +/− 50° swath width.
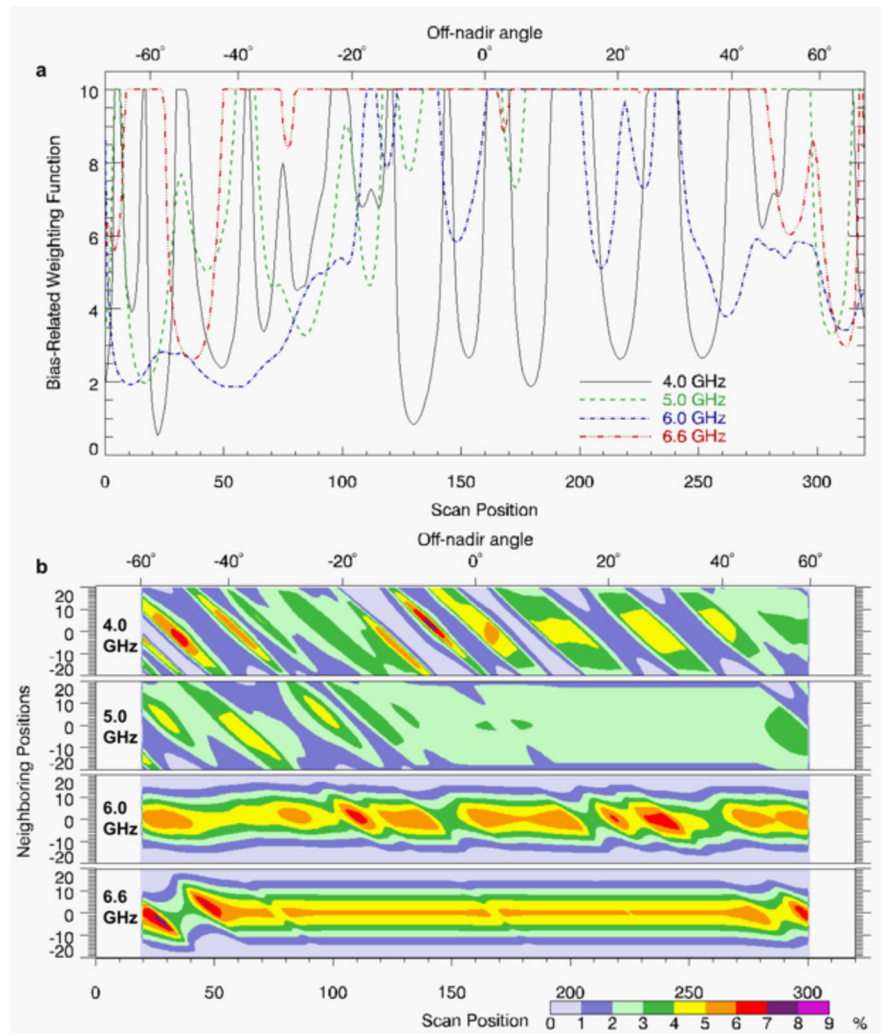
Figure 2.

(a) Weights derived from scan-position dependent relative biases for the flight leg in Fig. 1.
(b) Percentage contribution to the smoothed, filtered excess brightness temperature by neighboring pixels in each across-track scan, from the weights combined with the spatial Gaussian filter. The off-nadir angle (top axis) is the same as incidence angle, when aircraft pitch and roll are both zero.

Figure 3.
HIRAD footprint size as a function of off-nadir angle, before and after smoothing. An aircraft altitude of 20 km is assumed.
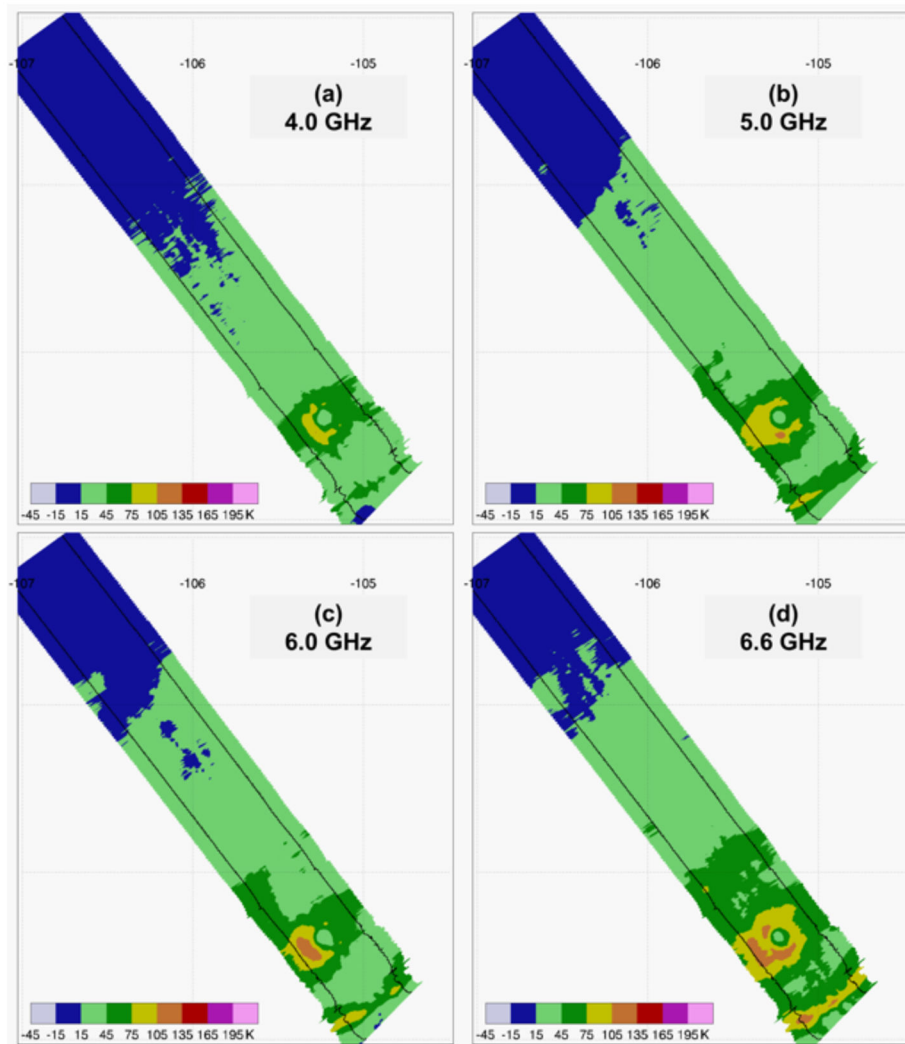
Figure 4.
As in Figure 1, but smoothed, filtered excess brightness temperatures.
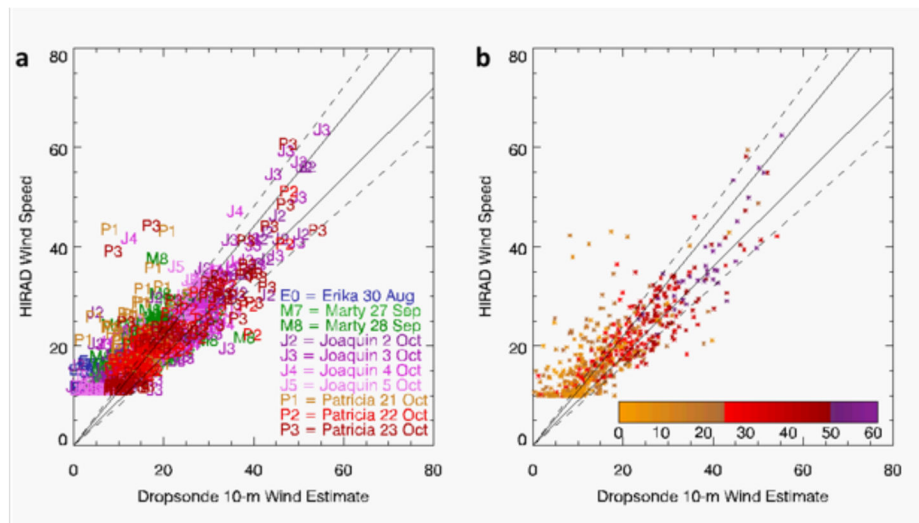
Figure 5.
HIRAD retrieved surface wind speed versus dropsonde-estimated surface wind speed. (a) Stratified by flight. (b) Stratified by HIRAD incidence angle. Solid lines mark +/−10% agreement; dashed lines mark +/−20% agreement.
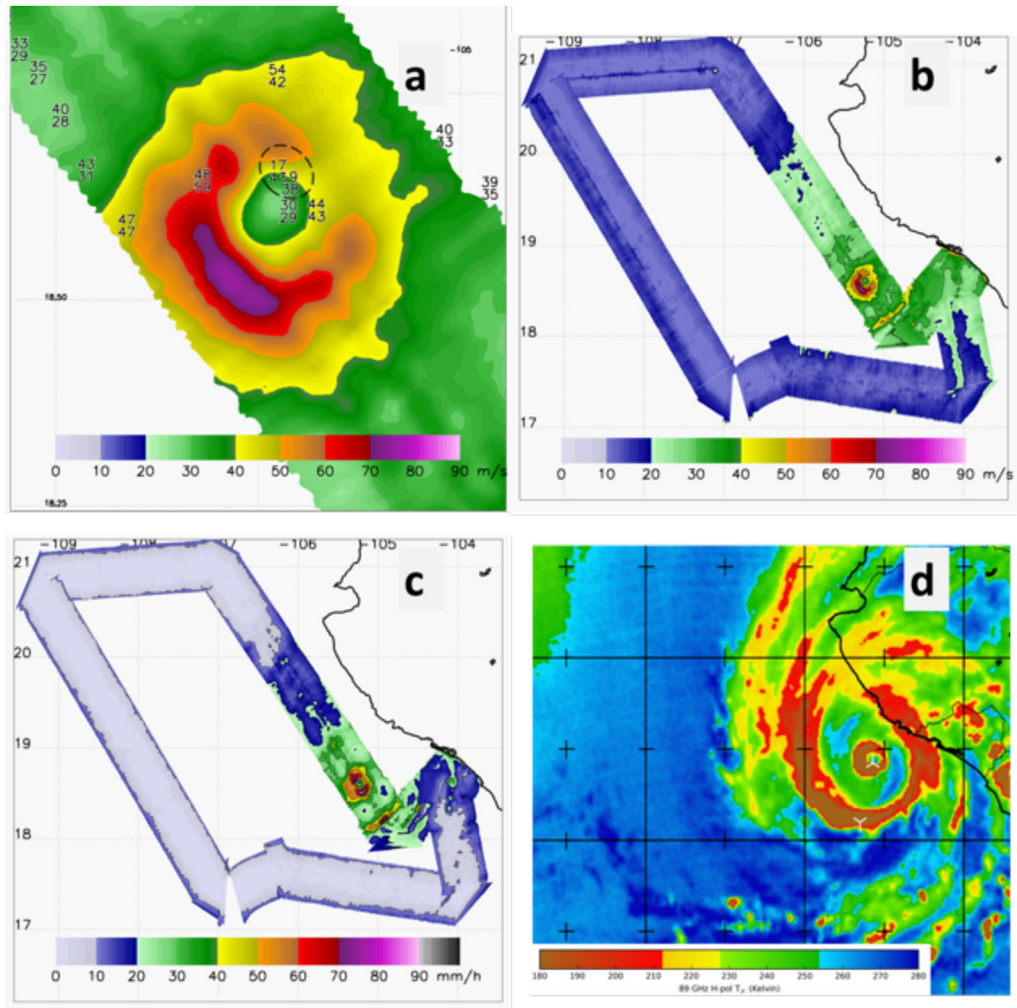
Figure 6.
(a) HIRAD retrieved wind speeds (m s^{-1}) for the +/−50° swath across the eyewall of Hurricane Patricia at 2001 UTC 23 Oct 2015. Printed numbers compare dropsonde (top numbers) versus HIRAD (bottom numbers) wind speeds at the dropsonde locations. Two dropsonde-HIRAD pairings discussed in the text are circled. Dropsonde trajectories and wind barbs overlaid on the HIRAD wind speed are shown in Rogers et al. (2017). (b) Wind speed (+/−60° swath) for all flight legs, 1946 – 2159 UTC. (c) Rain rate corresponding to (b). (d) AMSR-2 89 GHz horizontal polarization brightness temperature at 2027 UTC, image courtesy Josh Cossuth and the NRL Monterey TC web page team.
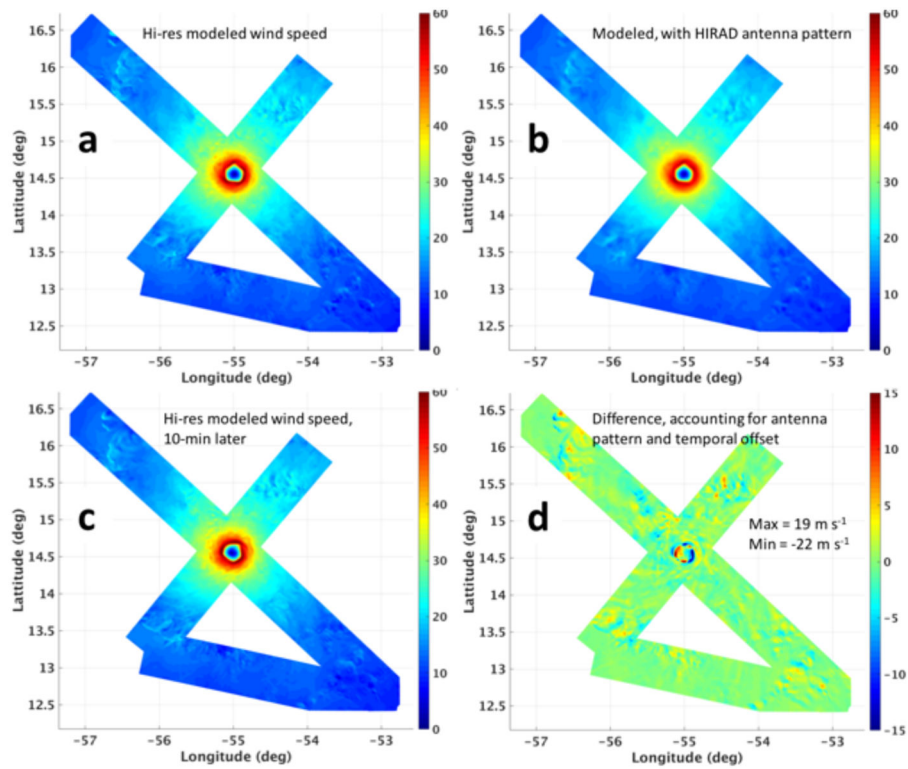
Figure 7.
(a) Surface wind speed (m s^{-1}) for a 1-km resolution idealized numerical model, with a hypothetical aircraft figure-4 pattern applied. (b) As in (a), but smoothed with HIRAD's antenna pattern. (c) As in (a), but 10 minutes later to simulate conditions encountered by dropsondes. (d) The difference (b) – (c).

Table 1

HIRAD measurement characteristics from a nominal 20 km altitude and 200 m s^{-1} forward motion, roughly consistent with WB-57 flights.

		Near nadir	40° off nadir	50° off nadir	55° off nadir
Swath width		-	33.6 km	47.7 km	57.1 km
Across-track sampling		0.1 km	0.2 km	0.4 km	0.6 km
Along-track sampling		0.2 km	0.2 km	0.2 km	0.2 km
Measurement footprint size (km × km)	4.0 GHz:	1.6 × 2.5	3.6 × 4.3	6.1 × 6.1	8.2 × 7.7
	5.0 GHz:	1.6 × 2.0	3.6 × 3.4	6.1 × 4.9	8.2 × 6.1
	6.0 GHz:	1.6 × 1.7	3.6 × 3.0	6.1 × 4.2	8.2 × 5.3
	6.6 GHz:	1.6 × 1.7	3.6 × 2.9	6.1 × 4.1	8.2 × 5.2
Effective footprint size *after smoothing* (km × km)	4.0 GHz:	1.6 × 2.5	3.8 × 4.5	7.2 × 6.8	11.3 × 9.3
	5.0 GHz:	1.6 × 2.0	3.7 × 3.5	6.3 × 5.0	9.6 × 6.6
	6.0 GHz:	1.6 × 1.7	3.7 × 3.0	6.5 × 4.4	9.1 × 5.6
	6.6 GHz:	1.6 × 1.7	3.6 × 2.9	6.6 × 4.3	10.0 × 5.8

Table 2

Sample size, bias, root mean square difference, and mean absolute difference for HIRAD comparisons with dropsondes, stratified by flights.

Flight	Sample size	Bias (m s⁻¹)		RMSD (m s⁻¹)		MAD (m s⁻¹)	
Post-Erika 30 Aug	46	5.7	47%	6.7	54%	5.7	47%
TS Marty 27 Sep	50	2.0	13%	4.4	28%	3.8	24%
Hurricane Marty 28 Sep	68	1.7	8%	5.8	28%	4.4	22%
Hurricane Joaquin 02 Oct	73	1.6	12%	5.7	30%	4.2	23%
Hurricane Joaquin 03 Oct	64	−0.1	2%	5.8	34%	4.7	26%
Hurricane Joaquin 04 Oct	73	0.0	2%	5.8	29%	4.0	21%
Hurricane Joaquin 05 Oct	65	2.5	17%	4.2	30%	3.1	20%
TS Patricia 21 Oct	57	5.5	21%	9.4	36%	6.5	28%
Hurricane Patricia 22 Oct	71	0.0	0%	4.4	23%	3.4	18%
Hurricane Patricia 23 Oct	69	−0.4	−3%	6.7	23%	4.1	17%
All	*636*	*1.6*	*11%*	*6.0*	*31%*	*4.3*	*24%*
Excluding 30 Aug, 21 Oct	*533*	*0.9*	*6%*	*5.4*	*28%*	*4.0*	*21%*

Table 3

As in Table 2, but stratified by HIRAD wind speeds below tropical storm (TS) strength, at tropical storm strength, and at hurricane strength.

HIRAD Wind Speed	Sample size	Bias (m s^{-1})		RMSD (m s^{-1})		MAD (m s^{-1})	
<TS: < 17.5 m s^{-1}	304	2.2	18%	4.5	36%	3.5	27%
TS: 17.5 – 33.0 m s^{-1}	279	0.8	3%	6.2	27%	4.7	21%
Hurricane: > 33.0 m s^{-1}	53	3.2	7%	10.7	26%	7.2	18%

Table 4

As in Table 3, but excluding Post-Erika 30 August, TS Patricia 21 October, and three dubious HIRAD-dropsonde matches in the eyes of Hurricanes Patricia and Joaquin.

HIRAD Wind Speed	Sample size	Bias (m s^{-1})		RMSD (m s^{-1})		MAD (m s^{-1})	
< TS: < 17.5 m s^{-1}	235	1.7	14%	4.1	33%	3.2	25%
TS: 17.5 – 33.0 m s^{-1}	248	−0.1	−1%	5.6	25%	4.3	19%
Hurricane: > 33.0 m s^{-1}	47	0.3	0%	6.3	16%	4.8	12%